3-D CFD-PBM coupled modeling and experimental investigation of struvite precipitation in a batch stirred reactor

Seyyed Ebrahim Mousavi, Mahbuboor Rahman Choudhury, Md. Saifur Rahaman

PII: S1385-8947(18)32575-0
DOI: https://doi.org/10.1016/j.cej.2018.12.089
Reference: CEJ 20629

To appear in: *Chemical Engineering Journal*

Received Date: 24 July 2018
Revised Date: 1 November 2018
Accepted Date: 17 December 2018

Please cite this article as: S.E. Mousavi, M.R. Choudhury, d.S. Rahaman, 3-D CFD-PBM coupled modeling and experimental investigation of struvite precipitation in a batch stirred reactor, *Chemical Engineering Journal* (2018), doi: https://doi.org/10.1016/j.cej.2018.12.089

3-D CFD-PBM coupled modeling and experimental investigation of struvite precipitation in a batch stirred reactor

Seyyed Ebrahim Mousavi, Mahbuboor Rahman Choudhury, Md. Saifur Rahaman*

Department of Building, Civil, and Environmental Engineering, Concordia University, 1455 de Maisonneuve Blvd, West, Montreal, Quebec, Canada H3G 1M8

*Corresponding Author: Email: saifur.rahaman@concordia.ca; Tel.: +1-514-848-2424, Ext. 5058.

Abstract

A general model has been developed to elucidate the precipitation of struvite crystals in a batch stirred tank reactor. The model, which evaluates reactor performance, also predicts crystal size distribution (CSD) over time by considering the hydrodynamic, thermodynamic, and kinetic aspects of solution in the reactor. A Computational Fluid Dynamics (CFD) model was coupled with Population Balance Modeling (PBM) to model the growth of crystals in the reactor. A thermodynamic equilibrium model for struvite precipitation was consolidated with the reactor model. While the equilibrium model provided information on supersaturation development, the coupled CFD-PBM model captured the crystal growth kinetics and the influence of the reactor hydrodynamics on the overall process. Size distribution is crucial as it determines distinct grades of final struvite crystals, which are to be used as commercial fertilizer. In the simulation, the CFD flow field was solved through a Eulerian multiphase approach and RNG-k-ε turbulence model. The population balance equation was solved using a discretized form of the continuous

partial differential equation, which transformed the continuous partial differential equation into finite ordinary differential equations as per size classes, which were then solved simultaneously. The growth rate, as a function of the supersaturation index (SI), was employed in the model through User Defined Function. The mean, standard deviation, and skewness of the model predicted CSD after 50 minutes were 20.81 μm, 9.61 μm, and 2.97, respectively and for the experimental CSD were 19.66 μm, 7.13 μm, and 2.46, respectively. The predicted peak-size percent fraction revealed a deviation from experimental results of 1.42%, 0.05%, 2.43%, 14.6%, 11.2%, 11.7%, 13.6%, and 14.2% at 0, 3, 10, 20, 30, 40, 50, and 60 min, respectively.

***Keywords*:** Struvite precipitation, Computational fluid dynamics, Population balance model, Stirred reactor, Growth rate

Nomenclature

A	Debye-Huckel constant	P	Pressure
$a(V,V')$	Aggregation kernel (m^3/s)	P_i	Impeller power (W)
B_{agr}	Birth rate due to aggregation	R_i	Production rate of i^{th} species
B_{brk}	Birth rate due to breakage	$\vec{r}$	Position vector
C_i	Ionic concentration	$\vec{R}_i$	Interphase momentum exchange
C_D	Drag coefficient	S_i	Source rate
$C_{1\varepsilon}$	k-e turbulence model parameter	$\vec{U}$	Velocity vector
$C_{2\varepsilon}$	k-e turbulence model parameter	$\vec{v_i}$	Phase velocity
C_μ	k-e turbulence model parameter	V	Volume
$\{C_i\}$	Ion activity of ion C_i	Y_i	Mass fraction of each species
D	Diameter (m)	Z_i	Valency of corresponding elements
D_{agr}	Death rate due to aggregation	S_i	Source rate
D_{brk}	Death rate due to breakage	$\vec{U}$	Velocity vector

D_m	Molecular diffusion	***Greek Letter***	
D_t	Turbulent diffusivity	α	Phase volume fraction
d_j	Diameter of solid particles	$\beta\ (V\|V')$	probability density function
d32	Sauter mean diameter (m)	γ_i	activity of solution
$\vec{F}_i$	Centrifugal forces	σ_k	k-e turbulence model parameter
f	Drag function	σ_ε	k-e turbulence model parameter
$G_{k,m}$	Generation of turbulent kinetic energy	ε	rate of turbulent energy dissipation (m^2/s^3)
$\vec{g}$	Gravitational acceleration (9.81 m/s^2)	θ	Azimuthal angle (degree)
$G(t)$	Growth rate	μ	viscosity (kg/m.s)
$g(V')$	Breakage frequency (s^{-1})	$\bar{\bar{\tau}}_{eff_i}$	Reynolds stress tensor (N/m^2)
I	Bulk fluid ionic strength	v	Number of daughter particles
$\bar{\bar{I}}$	Unit tensor	ρ	Phase density
Kg	Kinetic parameter	τ_j	Particulate relaxation time
Ksp	Struvite solubility constant	***Subscripts***	

K_{ij}	Interphase momentum exchange coefficient	agr	Aggregation
k	Turbulent kinetic energy (m^2/s^2)	brk	Breakage
M	Torque (Nm)	l	Liquid phase
N	Kinetic parameter	lam	Laminar
Np	Impeller power number	m	Mixture
$\vec{N}$	Angular velocity (rad/s)	s	Solid phase
$n(V, t)$	Number density depicting numbers of particle of size V at time t	t	Turbulent

1. Introduction

Discharge of significant amounts of phosphate from nutrient-rich wastewater is problematic considering the potential for contamination of groundwater and eutrophication of recipient water bodies. With an expected 40% rise in the world's population by 2050 [1] food consumption will increase rapidly in the near future, with consumption rates growing by 3.1% annually [2]. Without a doubt, naturally occurring phosphorous—found in the soil—cannot support this rapid growth in food demands. Consequently, augmenting soils with phosphorous-based fertilizers plays an indispensable role in permitting more food growth. Commercial fertilizers are produced primarily from phosphorous rock reserves, which are finite and non-

renewable in nature [3]. With increasing demands for phosphorous-based fertilizers all around the world, availability of phosphorous is expected to become scarcer and more expensive. As a result, phosphorus recovery is receiving increased amounts of attention as an alternative and cost-competitive option for the production of phosphorous-based fertilizers. Struvite produced from wastewater, which is known to provide an alternative source of both phosphorus and nitrogen, using a precipitation technique is a proven solution for phosphorus recovery and makes an interesting alternative for the fertilizer industry.

In the chemical precipitation method, which is the most widely used approach due to its operational simplicity, struvite precipitates from wastewater by addition of adequate amounts of Mg and by pH adjustment in the reactor to create alkaline conditions suitable for struvite precipitation. Small scale plants employ stirred tank reactors, as they are easy to run and control [4,5,14,6–13], while large-scale plants implement fluidized bed reactors, as they can provide higher reactive surface areas and better solution turbulence [15–19]. The present study employed a batch stirred reactor for a number of reasons, such as simplicity in setting up the experimental apparatus, shorter time required for each round of experimentation, and fewer reactant requirements.

Struvite precipitation depends on a variety of complex aspects such as fluid hydrodynamics, solution thermodynamics, mass transfer, and precipitation kinetics including the nucleation, growth, aggregation, and breakage of crystals [17,20–22]. Design and operation of an industrial scale crystallizer requires a reliable knowledge of these aspects, which have mostly been obtained from laboratory scale experiments. An efficient model that can predict different aspects of the process and combine these mechanisms in one unified theory is highly desirous, however to the authors' knowledge this has not been presented in the literature as of yet. Since

struvite is most commonly used as a commercial fertilizer, it may be useful that it is produced in a size-controlled manner to provide distinct grades for specific applications. Having size-controlled struvite production would help in post-production grading, handling, and commercialization of the fertilizers.

Struvite precipitation modeling studies fall into three major categories: hydrodynamic-focused models, thermodynamic-focused models, and kinetic-focused models. Most of the work completed in this field has covered one of these three mentioned aspects of the process. In hydrodynamic-focused models, researchers investigated the hydrodynamic behavior of the crystallizers in general. They focused on reactor configurations and studied the different parameters affecting the hydrodynamic behavior of reactor such as impeller speed, residence time, feed concentration and location, temperature [23,24,33,25–32]. Some studies modeled the thermodynamic aspect of the process using in-house codes or commercial thermodynamic solvers and investigated the thermodynamic parameters affecting struvite precipitation such as struvite solubility, species concentration, pH effect, and saturation state of the solution [34–38]. Kinetic-focused models attempted to determine the rate of struvite precipitation, which is the rate at which struvite constituent ions (magnesium, ammonium, and phosphate) get consumed to produce struvite. Such modeling can predict the variation of crystal size with time and/or optimized residence time and reactor volume. The predicted size can be regarded as the final struvite crystal size for a given time in a reactor volume. Some researchers suggested first-order kinetics and second-order kinetics for struvite precipitation [8,39–47]. One drawback of these proposed kinetic rates is that the nucleation and growth effect cannot be differentiated from the kinetic model and has an unknown combinational effect on growth and nucleation. In other studies, researchers investigated the precipitation kinetics based on an assumed growth rate or in

a few cases, nucleation and/or aggregation rate as a function of supersaturation state of the solution and reported order-dependency of the equation [20,22,48–53].

Few researchers have presented a holistic model that covers more than one aspect of the process and predicts crystal size distribution. Since crystal size is an important parameter in controlling the quality of produced struvite, the proposed model should accurately predict it. Ali and Schneider [20] estimated the crystal growth rate considering the thermodynamic aspect and power relation between growth rate, supersaturation index, and supersaturation ratio. By using their estimated coefficients, they predicted average particle size within a 10% margin of error, which is an acceptable level of prediction. Their work has limitations including assumption of a vigorous mixing in the system, which was deemed enough to overlook the hydrodynamic effect on the outcome and a lack of size distribution prediction. Hanhoun et al. [22] proposed kinetic rates for growth and nucleation using a population balance-based model coupled with a thermodynamic model. They predicted crystal size distribution (CSD) using a reconstruction model, which involved Laplace transformation of the number density function describing the CSD in a one-dimensional batch crystallization model [22,54,55]. The results, obtained by comparison between the crystal size produced during experiments (analyzed by laser granulometry and morphometry) and the values obtained by the numerical method of reconstruction of size distribution, show an under-prediction of the CSD with a significant percentage of error. The main limitations of this study are the ignoring of hydrodynamics in the process, overlooking of aggregation and breakage, and observation of a high degree of numerical deviations in the results. Galbraith and Schneider [56] developed a process model incorporating solution thermodynamics, nucleation, growth and aggregation mechanisms, and a population balance model (PBM) to simulate struvite precipitation. A series of experiments carried out by

Galbraith et al. [52], yielded an ensemble data set and this data set was used to regress the model's kinetic parameters for nucleation, crystal growth, and aggregation. A key limitation of this study was the uncertainty of the distribution of particles originating from the limitation of the experimental method. However, the limitation of the data obtained for parameter estimation was not essentially a limitation of the proposed model framework [52]. Rahaman et al. [17] presented a comprehensive mathematical model for a fluidized bed crystallizer including aspects of thermodynamics, precipitation kinetics, and reactor hydrodynamics in one model. Their results predicted removal efficiencies of constituent ions in an acceptable level of agreement with the experimental data. The model predicted the removal efficiencies of phosphate, ammonium, and magnesium with a maximum deviation of 9%, 3%, and 10%, respectively, when compared to the experimental observations [17]. They also predicted the average size of produced struvite crystals in the reactor. The study compared the average size of produced struvite crystals, obtained from model prediction, to that obtained from experiments and observed a 20-30% deviation in the model predicted values. Lack of size distribution prediction was a significant drawback for this work. Galbraith et al. [52] estimated the kinetic rate coefficient values for nucleation, growth, and aggregation rate using a data set generated from 14 batch experiments. Their model covers solution thermodynamics and particle development tracking through the application of a PBM. They predicted the time varying CSD by employing estimated kinetics rates. Prediction of size distribution within a 20-30% error range, as well as predicting the most common size at every time interval are important achievements of their work. Avoidance of the complexity of hydrodynamic effects by reducing their impact is the main limitation of their study.

A review of struvite precipitation literature shows the lack of a general model that presents particle size distribution of struvite by including all of the aspects mentioned above (i.e., hydrodynamic, thermodynamic, and kinetic) in one model. This study developed a 3-dimensional (3-D) computational fluid dynamics (CFD) model that integrates the kinetic rate resulting from the population balance equation with flow hydrodynamic and solution thermodynamic equations and predicts the variation of struvite particle size distribution over time for the first time. Development of such a holistic model may better enable design of efficient reactors and selection of operational parameters in reactors for the production of struvite crystals within a particular size range for use as commercial fertilizer.

2. Experimental Methodology

2.1 Solution Thermodynamics

Precipitation of Magnesium Ammonium Phosphate (MAP) hexahydrate ($MgNH_4PO_4.6H_2O$), commonly known as struvite, occurs via the following simplified chemical reaction:

$$Mg^{2+} + NH_4^+ + PO_4^{3-} + 6H_2O \rightarrow MgNH_4PO_4.6H_2O \quad (1)$$

Critically, supersaturation of the solution is the key to struvite precipitation. This parameter depends on solution pH and total elemental composition of reactive species. As multiple ions are involved in supersaturation in struvite case, defining solute concentration can be complex. To overcome this issue and to have a parameter to describe the state of supersaturation, solute concentration is defined in terms of the ion activity product (IAP), as detailed in the following equation:

$$\mathrm{IAP} = \{\mathrm{Mg}^{2+}\}\{\mathrm{NH}_4^+\}\{\mathrm{PO}_4^{3-}\} \quad (2)$$

Where $\{C_i\}$ represents the ion activity of ion C_i.

By defining IAP, the degree of supersaturation as described with the supersaturation index (SI) is as follows:

$$\mathrm{SI} = \log\left({}^{\mathrm{IAP}}/_{\mathrm{K_{sp}}}\right) \quad (3)$$

Where $\mathrm{K_{sp}}$ is the solubility product which shows the equilibrium state.

Therefore, when the IAP is less than $\mathrm{K_{sp}}$, the solution is unsaturated and when IAP is more than $\mathrm{K_{sp}}$, the system is supersaturated and nucleation or/and growth can occur. Over time, the system will ultimately return to an equilibrium state from a supersaturated state. The equilibrium solubility product used in this work is $\mathrm{K_{sp}} = 13.26$ [34] fixed at 25° C and atmospheric pressure.

Estimation of IAP for struvite has been made from the total initial molar concentrations of magnesium, nitrogen, phosphorus, and calculated equilibrium pH from charge balance. For this calculation, these species must be considered [17]: $\mathrm{MgPO_4^-}$, $\mathrm{MgHPO_4}$, $\mathrm{MgH_2PO_4^+}$, $\mathrm{Mg^{2+}}$, $\mathrm{MgOH^+}$, $\mathrm{H_3PO_4}$, $\mathrm{H_2PO_4^-}$, $\mathrm{HPO_4^{2-}}$, $\mathrm{PO_4^{3-}}$, $\mathrm{NH_4^+}$, $\mathrm{H^+}$, $\mathrm{OH^-}$, and $\mathrm{NH_3}$(aq). The corresponding equilibrium equations as well as thermodynamic constant values for these ions and complexes are provided in Table 1:

Table 1. Equilibrium constant for complexes

Equilibrium	**pK (25°C)**	**Reference**
$[\mathrm{Mg^{2+}}][\mathrm{PO_4^{3-}}]/[\mathrm{MgPO_4^-}]$	4.92	[57]

Equilibrium	pK (25°C)	Reference
$[Mg^{2+}][H_2PO_4^-]/[MgH_2PO_4^+]$	0.45	[58]
$[Mg^{2+}][\ HPO_4^{3-}]/[MgHPO_4]$	2.9	[59]
$[\ Mg^{2+}][OH^-]/[MgOH^+]$	2.56	[58]
$[H^+][H_2PO_4^-]/[H_3PO_4]$	2.15	[60]
$[H^+][HPO_4^{2-}]/[H_2PO_4^-]$	7.198	[60]
$[H^+][PO_4^{3-}]/[HPO_4^{2-}]$	12.375	[60]
$[NH_3][H^+]/[NH_4^+]$	9.3	[61]
$[H^+][OH^-]/[H_2O]$	13.997	[60]

Since analytical determination of magnesium, ammonia, and phosphate provide the total concentration of these species in solution, it is necessary to calculate ion activity by utilizing the appropriate activity coefficient and dissociation constants. The activity coefficient can be determined using a variety of empirical equations. Here, the Davies equation has been used to calculate the activity coefficient, since it is capable of performing activity calculations for higher ionic strengths [62]:

$$-\log \gamma_i = AZ_i^{\,2}\left[\frac{I^{1/2}}{1+I^{1/2}}\right] - 0.3I \qquad (4)$$

Where γ_i is the activity of solution, Z_i is the valency of corresponding elements, and A is the Debye-Huckel constant, which has a value of 0.509 at 25°C [62].

I is the bulk fluid ionic strength which can be calculated by the following defined relation, based on ionic concentration, C_i and respective charge, Z_i for all ions:

$$I = \frac{1}{2}\sum C_i Z_i^2 \quad (5)$$

Solving the above equations must be done with a numerical approach due to their complexity and non-linearity. In this work, a commercial spreadsheet software (Microsoft Excel 2003) was used to solve all of the equilibrium equations and constants in Table 1 along with the equations (1) to (5), based on iterative calculations for a given pH or SI. A Microsoft Visual Basic code was used in the Excel platform to perform the iterative calculation. This approach was previously used in Rahaman [63].

Considering struvite as a salt, the solubility at a given temperature depends on two major factors: species concentration and solution pH. The thermodynamic model results for minimum solubility pH in different initial concentrations verified by Olinger' solubility data [64] are presented in Figure 1. Together with the maximum threshold pH for the beginning of spontaneous nucleation of struvite derived from a series of experiments conducted by Ali and Schneider [65], Figure 1 is showing three zones for precipitation of struvite: (1) Unsaturated zone: crystals dissolve when added to the solution, and therefore, precipitation is impossible, (2) Metastable zone: the solution is saturated, and crystal growth can occur by seed addition, but the amount of Gibbs free energy is not enough for appreciable nucleation. However, nucleation depends on time and provided sufficient time, some nucleation might occur in this zone. Therefore, the growth phenomenon is predominant in this zone and (3) Labile zone or unstable zone: the solute concentration exceeds the equilibrium value considerably, and spontaneous nucleation can occur. Crystal growth can be rapid in this region.

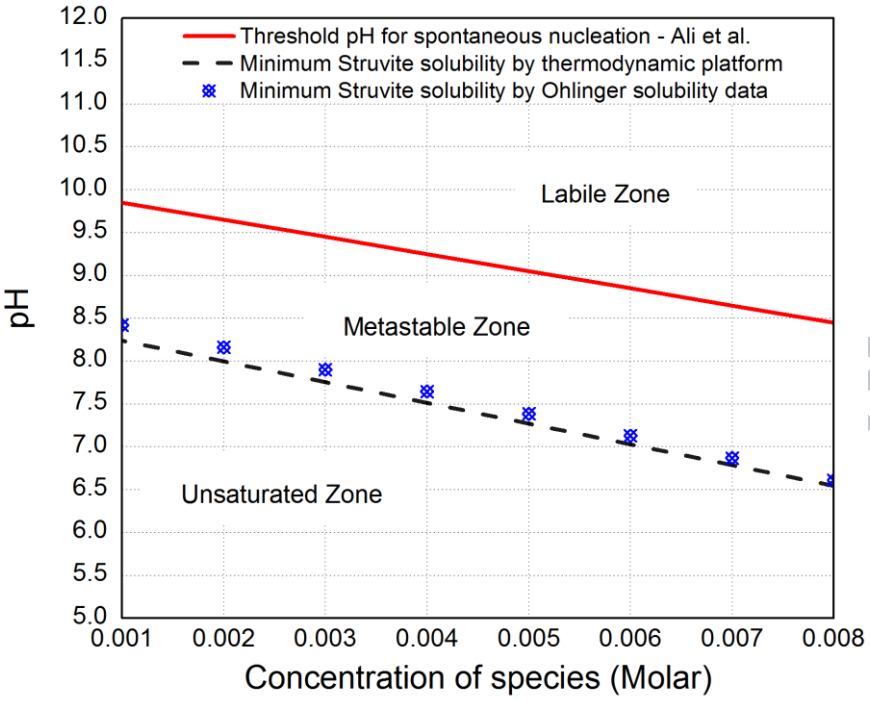

Figure 1. Determination of different saturation state zones for Struvite. Minimum struvite solubility (■) is collected from Ohlinger et al. [64] and threshold pH for spontaneous nucleation (—) is collected from Ali and Schneider [65].

The middle zone (zone between the red line and dashed line, in Figure 1) shows the operating zone for precipitation. The pH range between the minimum and maximum limit shows the metastable zone. Crystallization initiated by seed addition to the metastable zone is heterogeneous [65].

In this study, the initial molar concentration of species and solution pH were chosen in such a way that the initial state of solution stayed in the metastable zone. Precipitation occurring in this zone means that crystal growth is the dominant mechanism [48]. Also choosing the lowest possible pH in this zone will hinder crystal aggregation, as it has been reported that with increasing supersaturation, crystals are more adhesive and, accordingly, there is a higher chance

of crystal aggregation [66]. This approach assumes that mass transfer between the liquid phase and solid phase, which appears as a change in crystal size, occurs due to the growth of initial seeds while other phenomena, such as nucleation, have minimal effect.

2.2 Experimental Setup

The experimental work aims to determine the crystal size distribution at different time intervals. Batch experiments were performed, as this is easier in regards to parameter control. In a set of batch experiments, where distinct experiments are carried out, it is easier to control parameters such as temperature and pH during each experiment run. The experiments were carried out in a 1-L glass reactor with a round bottom (radius 142.5 mm), baffled with four removable, equidistant stainless steel baffles. Use of baffles improves the fluid mixing, avoids the creation of a dead zone occurring in the reactor, and also helps create a quick dynamic pH response. The reactor was well mixed with a Rushton impeller, rotating at a constant speed of 100 rpm in all experiments. The well-mixed reactor (BIO FLO 110, New Brunswick Scientific Co., Inc., Edison, NJ, USA) used in this study had inbuilt mechanisms for measuring the pH in the system and for keeping the temperature constant in the system. The BIO FLO 110 reactor's power requirements are 115 Volts, 50-60 Hertz, 20 VA. In this study, a synthetic solution containing the constituent elements of struvite was used. The reagents used in the preparation of the synthetic solution were Sigma ACS reagent grade $NH_4H_2PO_4$ and $MgCl_2.6H_2O$, and Milli-Q deionized (DI) water. Also, 0.5 M NaOH solution was used to adjust the pH. The temperature was held at 25ºC in all experiments.

2.3 Experimental Procedure

Different initial values of SI were selected in the experiments to keep the initial state of the batch reactor in the metastable zone to limit nucleation. First, the constituent ions were prepared by dissolving 0.005 M of Mg, N, and P in 1 L DI water. Through adjusting the pH by addition of 0.5 M NaOH, different initial pH and SI values were obtained, and a pH of 8 with corresponding SI value of 0.93 were chosen for the main experiment. For each experiment, the seed was prepared as described in section 2.5.

Samples of the crystals produced during the experiment had to be taken at different times to analyze the CSD. Having proper agitation in the reactor assures that each sample CSD is representative of the reactor. A pipette with an inlet diameter of 3 mm, which is very large considering the size range of the crystals measured in this study (10 – 120 μm), was used for sampling. A consistent and accurate sample volume (50 ml) was collected each time. For sampling during an experiment, the pipette tip was inserted to about mid-depth in the reactor and careful balance was maintained during the sampling to not touch the impeller blades or agitate the sample with the pipette tip. The present study did not perform any assessment on the variability of samples originating from the sampling methodology used. A particle size analyzer (PSA) was used to analyze each sample immediately after removal from the reactor. Non-return of the samples to the reactor did lead to a decrease in reactor volume, especially towards the end of experiment. Still, no samples were returned to the reactor as the entire experiment is a dynamic process, which involves continuous growth of crystals. Returning the sample to the reactor would have introduced some crystals that stayed outside the reactor in a different growth conditions and thus may have interfered with the representative CSD evaluation. In order to

avoid such interference and measure the CSD in this dynamic process at different time intervals, the samples were not returned in the reactor after collection for particle size analysis.

2.4 Measurements

A laser scattering particle size distribution analyzer form HORIBA (Model partica LA-950V2, Japan) was used to measure the crystal size distributions. The laser scattering PSA initially measures volume-based fractions in solution and then calculates number-based distribution of particles using the manufacturer's software. Use of a laser scattering particle size analyzer may lead to large errors, especially on the small end of size range, due to lack of resolution in analysis. The detection range of this machine ranges from 10 nm to 3 mm, which covers the expected particle size range in this work. Also, the lower range of measurement may not be valid for experimental conditions in case nuclei formation takes place. pH measurement was performed by a Mettler Toledo pH probe (Model 405-DPAS-SC-K8S/225, USA).

2.5 Seed Preparation

As the initial solution is in the metastable zone, the experiments were seeded to limit primary nucleation. To uniformly disperse seeds, wet seeding was chosen. To prepare the seed, 0.005 mol of $NH_4H_2PO_4$ and $MgCl_2.6H_2O$ were dissolved in 1L DI water and the whole system was stirred with a magnetic stirrer. Then, 0.5 M NaOH was added to raise the pH until the first precipitation of crystals was detected visually. The NaOH was incrementally added and a final volume of about 3-4 ml was added in different trials to visually observe precipitation. Then the solution was filtered and the crystals were dried overnight in a glass desiccator at room temperature (22±2 ^{o}C) in order to measure the distribution of seed crystal size, which shows the initial size distribution of particles, 4 random samples were collected from the dried seed stock

and then dispersed in 4 tubes containing DI water with a pH of 8.5. The pH of the DI water was kept alkaline (pH 8.5) to avoid any dissolution of struvite crystal in solution. The seed had a solid concentration of 3 g/L and was sonicated for 5 min to make sure that no substantial aggregation between the seed particles took place and was reflected in the CSD measurement. The Branson Digital Sonifier 450 (Branson Ultrasonic Corp., Danbury, CT, USA) was used to sonicate the solution. The power output of the sonifier is up to 400 watts at 100% amplitude. In this study, the solution was sonicated at 70% amplitude for 5 min. Although the present study did not perform any parametric studies to assess influence of sonication time on aggregation between seed particles, the impact of the 5 min of sonication was assumed to be sufficient to prevent significant aggregation between the seed particles. CSD measurement was performed for all four of the random samples and the average was chosen as the initial size distribution for seed. Figure 2 shows the CSD results for four samples and the average chosen as the initial size distribution for seed.

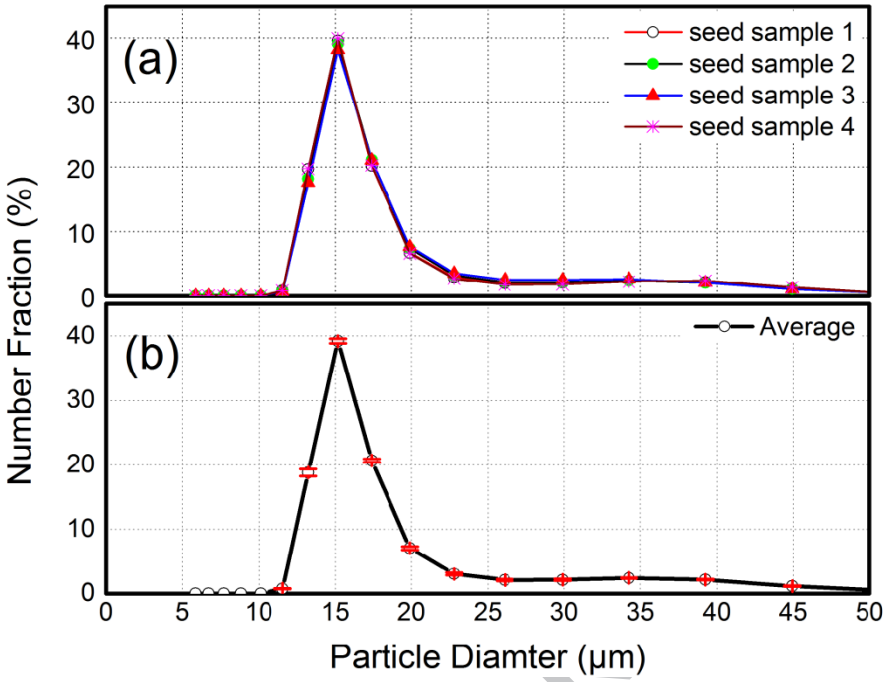

Figure 2. Number-based initial crystal size distribution (CSD) of seeds, (a) 4 random samples and (b) average initial CSD used in the CFD model

3. CFD Modeling

3.1 Mathematical Modeling and Governing Equations

The mathematical model of liquid-solid flow was developed via the 3D Eulerian multiphase approach. In the Eulerian approach, the two phases are considered mathematically as interpenetrating continua. As the two phases occupy separate volumes in the same 3-D space, the concept of volume fraction is valid, and these two sets of equations are closed by constitutive relations or by the application of kinetic theory.

Continuity Equation

Most of the processes taking place in a stirred tank reactor are under a turbulent regime. Therefore, the Reynolds averaged mass and momentum equations must be considered. The continuity equation for each phase is as follows:

a) For liquid phase:

$$\frac{\partial}{\partial t}(\rho_l \alpha_l) + \nabla.(\rho_l \alpha_l \vec{U}_l) = 0 \quad (6)$$

b) For solid phase:

$$\frac{\partial}{\partial t}(\rho_s \alpha_s) + \nabla.(\rho_s \alpha_s \vec{U}_s) = 0 \quad (7)$$

Where α_l is the volume fraction of liquid phase, α_s is the volume fraction of solid phase, ρ is the density, and $\vec{U}$ is the velocity vector.

The liquid phase l and solid phase s are assumed to share the whole space in proportion to their volume such that sum of their volume fractions is equal to one:

$$\alpha_l + \alpha_s = 1 \quad (8)$$

Momentum equation

The momentum conservation equation for each phase is written as:

a) For liquid phase:

$$\frac{\partial}{\partial t}\left(\rho_l \alpha_l \vec{U}_l\right) + \nabla.\left(\rho_l \alpha_l \vec{U}_l \vec{U}_l\right) = \alpha_l \nabla p + \nabla.\bar{\bar{\tau}}_{eff_l} + \vec{R}_l + \vec{F}_l + \rho_l \alpha_l \vec{g} \quad (9)$$

b) For solid phase:

$$\frac{\partial}{\partial t}\left(\rho_s \alpha_s \vec{U}_s\right) + \nabla.\left(\rho_s \alpha_s \vec{U}_s \vec{U}_s\right) = \alpha_s \nabla p + \nabla.\bar{\bar{\tau}}_{eff_s} + \vec{R}_s + \vec{F}_s + \rho_s \alpha_s \vec{g} \quad (10)$$

Where p is the pressure shared by the two phases and $\vec{R}_i$ represents the interphase momentum exchange terms. The interphase momentum transfer is due to interfacial forces acting and interactions between water and solid particles.

The term $\vec{F}_i$ represents the centrifugal force and Coriolis acceleration force term applied rotation and is written as:

$$\overrightarrow{F_i} = -2\alpha_i \rho_i \vec{N} \times \overrightarrow{U_i} - \alpha_i \rho_i \vec{N} \times (\vec{N} \times \vec{r})$$

(11)

The Reynolds stress tensor $\bar{\bar{\tau}}_{eff_i}$ is based on the mean velocity gradients using the Boussinesq hypothesis:

$$\bar{\bar{\tau}}_{eff_i} = \alpha_i\left(\mu_{lam,i} + \mu_{t,i}\right)\left(\nabla\overrightarrow{U_i} + \nabla\vec{U}_i^T\right)$$

$$-\frac{2}{3}\alpha_i\left(\rho_i k_i + \left(\mu_{lam,i} + \mu_{t,i}\right)\nabla.\overrightarrow{U_i}\right)\bar{\bar{I}} \quad (12)$$

Where $\mu_{lam,i}$ is the laminar viscosity of ith phase and $\mu_{t,i}$ is the turbulent viscosity of ith phase.

Interface momentum exchange

The two phases interact through momentum transfer term [equations (9) and (10)]. This momentum exchange occurs through interfacial forces acting on liquid and solid. These forces- considered as sources or sinks in the momentum equation-must be formulated separately.

In this work a simple form of interaction has been used to solve the interphase force:

$$\sum_{j=1}^{n} \overrightarrow{R_{ji}} = \sum_{i=1}^{n} K_{ji} \left(\overrightarrow{v_i} - \overrightarrow{v_j}\right) \quad (13)$$

Where $\overrightarrow{v_i}$ and $\overrightarrow{v_j}$ are the phase velocities and $K_{ji} = K_{ij}$ is the interphase momentum exchange coefficient, which can be written in the following equation:

$$K_{ji} = \frac{\alpha_i \alpha_j \rho_j f}{\tau_j} \quad (14)$$

Where τ_j is particulate relaxation time defined as:

$$\tau_j = \frac{\rho_j d_j^2}{18\mu_i} \quad (15)$$

Where d_j is the diameter of solid particles.

And f is the drag function, which contains the drag coefficient C_D. There are different drag models used throughout the literature and the difference between them relies on the difference between the ways they are calculating this f function. Between different drag models, Syamlal-O'Brien offers more accurate results in this type of study as compared to the other methods [67].

The Syamlal-O'Brien model:

$$f = \frac{C_D Re_s \alpha_l}{24 v_{r,s}^2} \quad (16)$$

Drag coefficient derived by Dalla Valla:

$$C_D = \left(0.63 + \frac{4.8}{\sqrt{Re_s / v_{r,s}}}\right)^2 \quad (17)$$

In this model, based on measurements of the terminal velocities of particles in settling or fluidized beds, the relative Reynolds number can be derived, which has a correlation with volume fraction:

$$\mathrm{Re_s} = \frac{\rho_l d_s |\overrightarrow{v_s} - \overrightarrow{v_l}|}{\mu_l} \tag{18}$$

Where l is for the liquid phase, s is for the solid phase, and $d_s$is the diameter of the solid phase particles.

Turbulence modeling – RNG k - ε model

In this work, the renormalized group k-ε model was used. For the continuous phase—liquid phase in this study—the RNG k-ε model was used and the governing equations are written as below:

$$\frac{\partial}{\partial_t}(\rho_m k) + \nabla . (\rho_m \overrightarrow{v_m} k) = \nabla . \left(\frac{\mu_{t,m}}{\sigma_k} \nabla k\right) + G_{k,m} - \rho_m \varepsilon \tag{19}$$

$$\frac{\partial}{\partial_t}(\rho_m \varepsilon) + \nabla . (\rho_m \overrightarrow{v_m} \varepsilon) = \nabla . \left(\frac{\mu_{t,m}}{\sigma_\varepsilon} \nabla \varepsilon\right) + C_{1\varepsilon} G_{k,m} - C_{2\varepsilon} \rho_m \varepsilon \tag{20}$$

Where $G_{k,m}$ is generation of turbulent kinetic energy due to the mean velocity gradients. The effective turbulent transport varies with the effective Reynolds number (or eddy scale) allowing the model to better handle low-Reynolds number and near-wall flows. In the high-Reynolds number, as used this work, turbulence viscosity of the ith phase calculated form

$$\mu_{t,m} = \rho_m C_\mu \frac{k^2}{\varepsilon} \tag{21}$$

Where C_μ is constant. Other fundamental turbulent flows model constant values have been determined from previous experiments. The most widely accepted standard values for these constants are as follows [67]:

$$C_{1\varepsilon} = 1.44\,, C_{2\varepsilon} = 1.92\,, C_\mu = 0.09\,, \sigma_k = 1.0\,, \sigma_\varepsilon = 1.3$$

Species transport equation

The conservation equation for the i[th] species is

$$\frac{\partial}{\partial_t}(\rho Y_i) + \nabla\,.\,(\rho V_k Y_i) = \nabla\,.\left(\rho D_m + \frac{D_t}{Sc_t}\right)\nabla Y_i + R_i + S_i \tag{22}$$

Where Y_i is the i[th] species mass fraction, Sc_t is turbulent Schmidt number, D_t is the turbulent diffusivity, D_m is molecular diffusion, R_i is the rate of species *i* production by chemical reaction, and S_i is the rate of addition by any extra sources. The default Sc_t number is 0.7 [68].

Population balance equations

The population balance equation (PBE) provides a simple form of population continuity for any phenomena. It can be derived as a balance for particles in a physical space. The general form of PBE is defined as:

$$\frac{\partial}{\partial_t}[n(V,t)] + \nabla.[\vec{u}n(V,t)] = B_{agr} - D_{agr} + B_{brk} - D_{brk} \tag{23}$$

Where D_{agr} and B_{agr} are death rate and birth rate of particles, respectively, of volume V due to aggregation, while D_{brk} and B_{brk} represent the death rate and birth rate of particles of volume V due to breakage, respectively. Aggregation rate and breakage rate are defined as follows:

$$B_{agr} = \frac{1}{2}\int_0^V a\,(V - V', V')n(V - V')n(\,V')dV' \tag{24}$$

$$D_{agr} = \int_0^{\infty} a\,(V, V')n(V)n(V')dV' \quad (25)$$

$$B_{brk} = \int_{\Omega_v} vg\,(V')\beta\,(V|V')n(V')dV' \quad (26)$$

$$D_{brk} = g(V)n(V) \quad (27)$$

As D_{agr} and B_{agr} describes the aggregation rate and D_{brk} and B_{brk} describes the breakage rate. To link population balance modeling of the secondary phase with fluid dynamics, Sauter mean diameter (d_{32}) will be calculated by the ANSYS Fluent and used to represent the particle diameter of the solid (secondary phase) in each calculation step. Sauter mean diameter can be obtained from:

$$d_{32} = \frac{\sum n_i d_i^3}{\sum n_i d_i^2} \quad (28)$$

Which illustrates the diameter of a sphere in a collection of equisized spherical objects that has the same "*volume/surface area*" ratio as the collection of polysized particles in the system. In this work, for solving the PBE the discretized method, also known as the method of classes or sectional method, which was developed by Ramkrishna [69], Hounslow et al. [70] and Lister et al. [71], is implemented. In this method, the continuous particle population is discretized into a finite number of size intervals or bins. Although this approach has the advantage of computing particle size distribution directly, it requires *a priori* knowledge of the bin sizes and may need a large number of classes to cover the whole range of particle sizes. The size intervals or bins were fixed on the basis of experimental size ranges obtained from the PSA. The PSA provided us CSD on the basis of different size ranges. We selected 25 size ranges, which encompass all the experimental CSD observations in this study. 25 size classes—the exact same sizes as reported

by PSA—have been applied to the model through a probability density function (PDF) file to cover the entire potential range of particle sizes.

Growth rate

Crystal growth rate can be described as a function of the solution supersaturation index SI (defined earlier) as follows:

$$G(t) = {}^{dl}/_{dt} = k_g \, SI^n \quad (29)$$

Where k_g and n are the kinetic coefficients. The difference in solubility of the various faces of a single crystal, or of different size particles of the same material, are not large enough to influence crystal growth unless the crystals are less than 1 μm [72]. Therefore, we assumed that the struvite crystals suspended in the solution grow at a similar rate. In this work, as explained earlier, the initial solution was prepared in a way that the solution was in the metastable zone so that crystallization was not governed by nucleation. Therefore, the kinetic model has been selected based on the assumption that nucleation and aggregation are negligible and a growth rate was used. The values of the coefficients (k_g and n) were taken from the average of the ranges as reported by Ali and Schneider [20]. The exact values of k_g and n used in this study were 48 μm/h and 1.66, respectively, and the growth rate was added into the simulation through User Defined Function (UDF).

3.2 Solution Domain, Mesh and Boundary Conditions

The same reactor, as used in the experiment, was modeled in simulation. The reactor was built of glass and had a diameter of 124 mm and a height of 90 mm. The bottom radius of the reactor is 142.5 mm. A standard six-blade Rushton turbine impeller agitated the reactor. The

clearance between the centrally located impeller and the bottom of reactor was held at 35 mm. Further geometric details are provided in Figure 3.

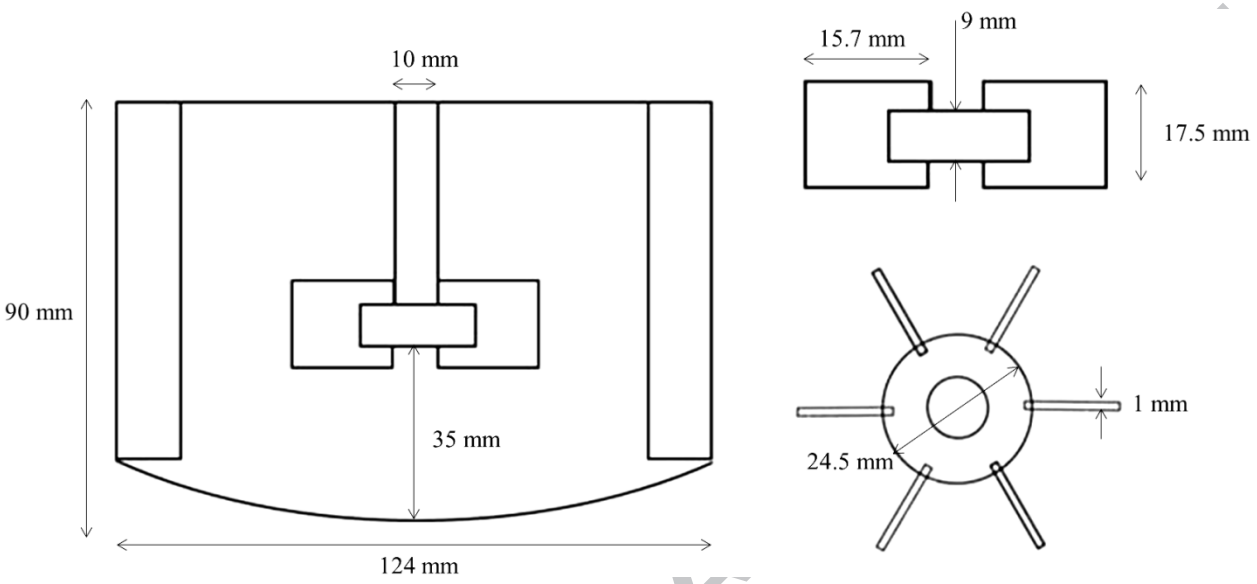

Figure 3. Schematic views of the reactor geometry and impeller used for this study

No slip wall boundaries were set to all walls. For the reactor upper surface, pressure outlet was assumed as fixed to the local atmosphere. As it is important in such modeling to employ an adequate number of computational cells, the geometry divided into more than 2×10^5 3-D tetrahedral computation discrete control volumes or cells by the commercial grid generation tool, ANSYS Workbench v.17.1. To assure that the results were independent of the mesh size, four different tetrahedral grid configurations were chosen to check mesh independency. Also, in order to capture the complex flow behavior around both the impeller tip and at the baffle edges, a refinement factor was used in these regions. The difference between these four grids resulted from the grid size and the refinement factor used, as seen in Table 2.

3.3 Method of Solution

Modeling the impeller rotation is complex as there is relative motion between the stationary baffles and rotating impeller blades. The two most common approaches for this type of modeling are the Multiple Reference Frame (MRF) and Sliding Mesh (SM) models. In these models, the solution domain is divided into two main regions: (1) Rotor: inner region containing the rotating impeller and (2) Stator: outer region containing the stationary baffles and vessel walls. For the MRF model, steady-state calculations are performed with a rotating frame of reference in the impeller region and a stationary frame of reference in the outer region. For the SM model, the impeller region slides relative to the outer region in discrete time steps and time-dependent calculations are performed using implicit or explicit interpolation of data at consecutive time-points. Although the SM method is more accurate for the modeling of actual phenomenon such as impeller rotation as it is time dependent, it is computationally demanding. In this work, the MRF method was used and the MRF zone was created around the Rushton blades and the shaft as shown in Figure 4.

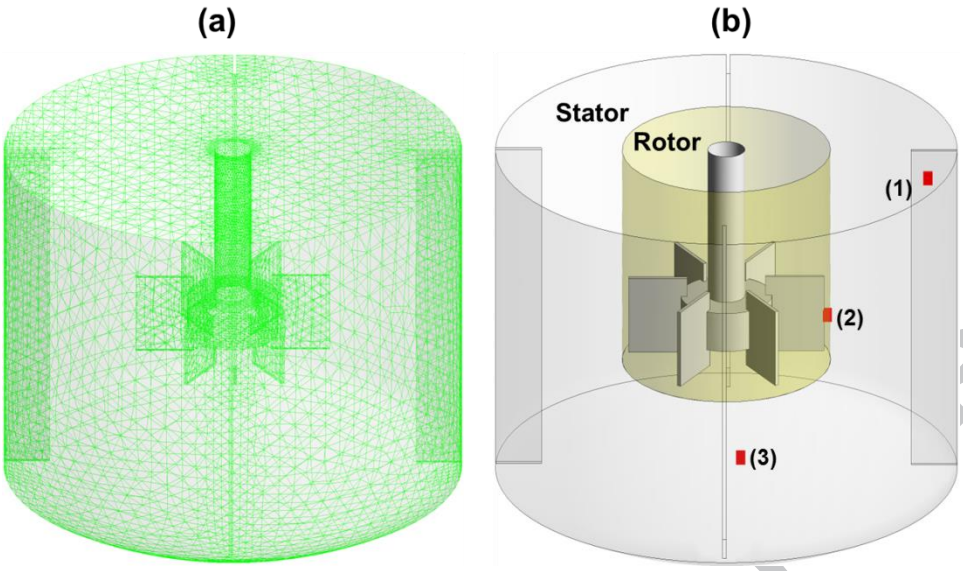

Figure 4. 3D Schematic view of the reactor domains (a) computational grids employed, (b) MRF zones and selected points for mesh independency check. The selected points for mesh independency check are (1) a point near the top of one stationary baffle in the stator zone, (2) a point on the middle-outside edge of a rotating blade of the impeller in the rotor zone, (3) a point on the bottom wall of the reactor below the impeller in the stator zone.

In this work, all computational work was performed in double precision mode using the commercially available CFD code package, ANSYS Fluent v.17.1. The pressure-based solver is used to numerically solve the continuity and momentum equations for velocity and pressure fields. A coupled SIMPLE scheme was chosen for the pressure-velocity coupling method. This algorithm uses a relationship between velocity and pressure correction to enforce conservation of continuity and to attain the required pressure field. All governing equations, described earlier, were discretized by ANSYS Fluent software using the finite volume approach with a First-Order upwind discretization scheme. Then, an Eulerian multiphase method implemented in the software was applied. Liquid phase was considered the continuous phase (primary phase) and the

solid was considered the dispersed phase (secondary phase). The time step size used in the model was initially 0.001s and, as the solution converged, the time step size was gradually increased to 0.01s to save computational time. The total computational time was about 8 weeks for simulation of 60 minutes (3600 seconds) of physical time. All calculations were performed with 48 paralleled processors in the high-performance computing facilities of CalculQuebec and ComputeCanada.

4. Results and Discussion

4.1 Grid Independence Results

Four different grid configurations were chosen to understand the influence of mesh configuration on the flow prediction. The detailed profile for each grid case and the grid study results are presented in Table 2.

Table 2 Different applied grids and number of cells

Grid Case No.		**1**	**2**	**3**	**4**
Number of cells		1.9×10^5	2.2×10^5	3.5×10^5	4.5×10^5
Grid size (mm)		5.5	5	5	4
Refinement factor	around baffles	1	1	1	1
	around impeller	1	1	2	2
Liquid phase velocity at point (1) (m/s)		0.0153	0.0266	0.0282	0.0288
Liquid phase velocity at point (2) (m/s)		0.233	0.256	0.259	0.260
Liquid phase velocity at point (3) (m/s)		0.0680	0.0764	0.066	0.0571

Average Liquid phase velocity (m/s)	0.0619	0.0623	0.0624	0.0625

The liquid phase velocity at three different points (points 1, 2, and 3) shown in Figure 4 and the volume-averaged liquid phase velocity over the whole domain were chosen to study the grid sensitivity of the model. As the differences between numerical results in grid case no. 2, 3 and 4 were not very high in most cases when compared to the same differences observed with grid case no. 1; grid case no. 2 was chosen for the simulation in this study as it runs faster.

4.2 Flow Pattern Prediction Validation

For any CFD simulation, it is desirable to validate the CFD prediction of the flow field before commencing any further steps. In this work, this validation was performed by experimental results of other researchers. Geometry-independent parameters such as impeller power number, overall flow pattern, and velocity magnitude distribution were chosen as parameters to validate the hydrodynamic behavior of the CFD model.

Impeller power number validation

The impeller power number Np has been commonly used to check the validity of CFD simulation of single phase flow in stirred tanks [73–75]. In this work, simulation was conducted for both single phase flow (water) and multiphase flow (mixture) as a validation technique for multi-phase flow, and power results were compared with experimental values reported by Rushton et al. [76]. Power numbers were calculated from the model prediction torque for a wide range of Reynolds numbers, from laminar to turbulent flow regimes, and based on the following equations:

$$R_e = \frac{\rho N D_I^2}{\mu} \quad (30)$$

Where ρ is the density (kg/m^3), μ is viscosity (kg/m.s), D_I is the tip-to-tip impeller diameter and N is the impeller speed (S^{-1}).

$$P_i(W) = 2\pi N(s^{-1}) M\ (Nm) \quad (31)$$

Where, P_i is the power needed for rotating the impeller (W), N is the speed of rotation (s^{-1}) and M is the torque (Nm). The power numbers were then calculated as dimensionless numbers to generalize power factor for any case as follows:

$$N_p = \frac{P_i\ (W)}{\rho\ (kgm^{-3})\ N\ (s^{-1})^3\ D(m)^5} \quad (32)$$

Where ρ is the fluid density (kgm^{-3}) and D is impeller diameter (m). It should be pointed out that for Reynolds number less than 10, equation (32) is not valid.

To cover a complete range of fluid regimes, the simulation starts with Reynolds number = 10 and a corresponding speed of 0.2 rpm. The other Reynolds numbers were simulated, by changing the speed of agitation. Reynolds numbers of 10, 100, 200, 1000, 5000, 10000, 25000, and 50000 were simulated. For the turbulent regime, the RNG k-ε model was chosen, as it is used for further steps, and for Reynolds numbers lower than 200, laminar flow was chosen since Reynold number = 200 is the boundary of laminar flow in stirred tanks with Rushton impellers [77]. The results for this comparison are shown in Figure 5.

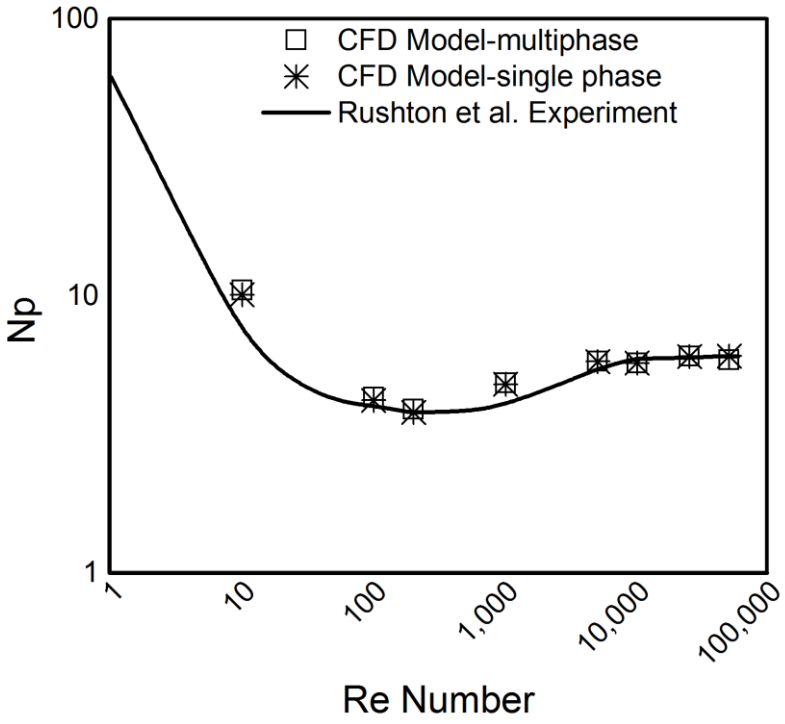

Figure 5. Comparison of experimental and CFD model (single phase and multiphase) predicted impeller power number with experimental data provided by Rushton et al. [76]**.**

As is apparent, the model prediction for single phase flow is in agreement with the Rushton et al. [76] experimental data. In this study, the single phase and multiphase simulation results were obtained using a round-bottomed reactor. The reactor had a rounded bottom with a large radius (142.5 mm) as compared to the height and diameter of the reactor. As a result, the height of the bottom-curved part (15.3 mm) was not very large as compared to the overall height of the reactor (90 mm). It can be hypothesized, though not determined here, that the impact of a large-radius curved bottom, which constituted a small part of the total reactor height, offered minute deviations in power number prediction for different Re number when compared to the results obtained with a flat bottom reactor by Rushton et al [75]. In addition to this, errors in extraction of numerical data from a graph in the original Rushton et al. [75] paper, using a web-

based plot digitizer, may have led to some errors in the plotting of the solid line in Figure 5. Since both these axes are in logarithmic scale, a small deviation might result in more agreement to the predicted data obtained in this study. Nevertheless, the predicted data showed similar trends to those observed by Rushton et al. [75]. Similar results obtained for multiphase flow show satisfactory agreement with the single-phase results, as well as experimental data. This correspondence in the single phase and multiphase flow results was expected since the solid volume fraction in this work is in the range of 10^{-5}. Although in the present study a two-phase system was modeled due to the presence of a solid fraction and a liquid fraction in the reactor, it can be argued that a single-phase model could have also sufficed for similar result output under such solid volume fraction scenario. The highest percentage of deviation (~17%) occurred at Re = 10. A possible reason for this discrepancy is the effect of baffles used for development of mixing conditions which can disturb the laminar flow regime in Reynolds number = 10.

Overall Flow Pattern

An assessment for the accuracy of the CFD model in predicting flow field could be conducted by comparing the velocity vector configuration with the laser Doppler velocimetry (LDV) results of previous studies. Costes and Couderc [78] investigated the hydrodynamic characteristics of the flow induced by a standard Rushton impeller. They reported mean velocities in two vertical planes; the median plane between two baffles ($\theta = 45^{\circ}$) and the plane of the baffles ($\theta = 0^{\circ}$). Figure 6 (E1/CFD1 and E2/CFD2) shows the CFD model velocity prediction in comparison with Costes and Couderc [78] results in the plane of baffles and in a median plane between two baffles, respectively.

The circulation pattern of the flow is correctly reproduced. The position of the recirculation centers is in accordance with the experimental results, showing that as we expected,

Rushton turbine is a radial flow type of impeller, as the axial velocity components are almost vertical at the top of the blades. Also, the intensity and direction of the radial flow jets from impeller tip toward the reactor walls were also correctly predicted.

It is important to note that the flow pattern and recirculation arrangement are quite independent of the stirrer speed and of the size of the reactor as reported by Costes and Couderc [78] and also the qualitative nature of the multiphase flow field around the impeller and shape of the flow jet is similar to that of single phase flow, especially for low solid concentration as investigated by Wadnerkar et al. [79].

Another parameter, which a CFD model should be able to predict, is the velocity magnitude distribution in a stirred tank. Here, the contour for the velocity is shown in Figure 7, which presents the velocity profile as predicted by the CFD model. As expected, velocity magnitude decreases according to the increased radius and the highest magnitude velocity occurs at the impeller tip. Contour plots of the solid volume fraction in the reactor (at minute 60) on a vertical symmetry plane and three different horizontal planes located at 20 mm, 50 mm, and 80 mm from the bottom of the reactor are shown in Figure S1 (Supporting Information). It can be observed that, for most part, the inhomogeneity in the solid phase volume fraction of the reactor fell within a narrow range between 3.90×10^{-5} to 4.55×10^{-5}. Larger solid phase volume fractions were present in the zone below the rotating impeller (Figure S1) due to the low velocity in that region. The initial overall solid volume fraction of the dispersed phase was 1.47×10^{-5} when the seed crystals were introduced to the reactor. At the end of 60 min, the solid volume fraction of the dispersed phase increased by about three times to 4.32×10^{-5}.

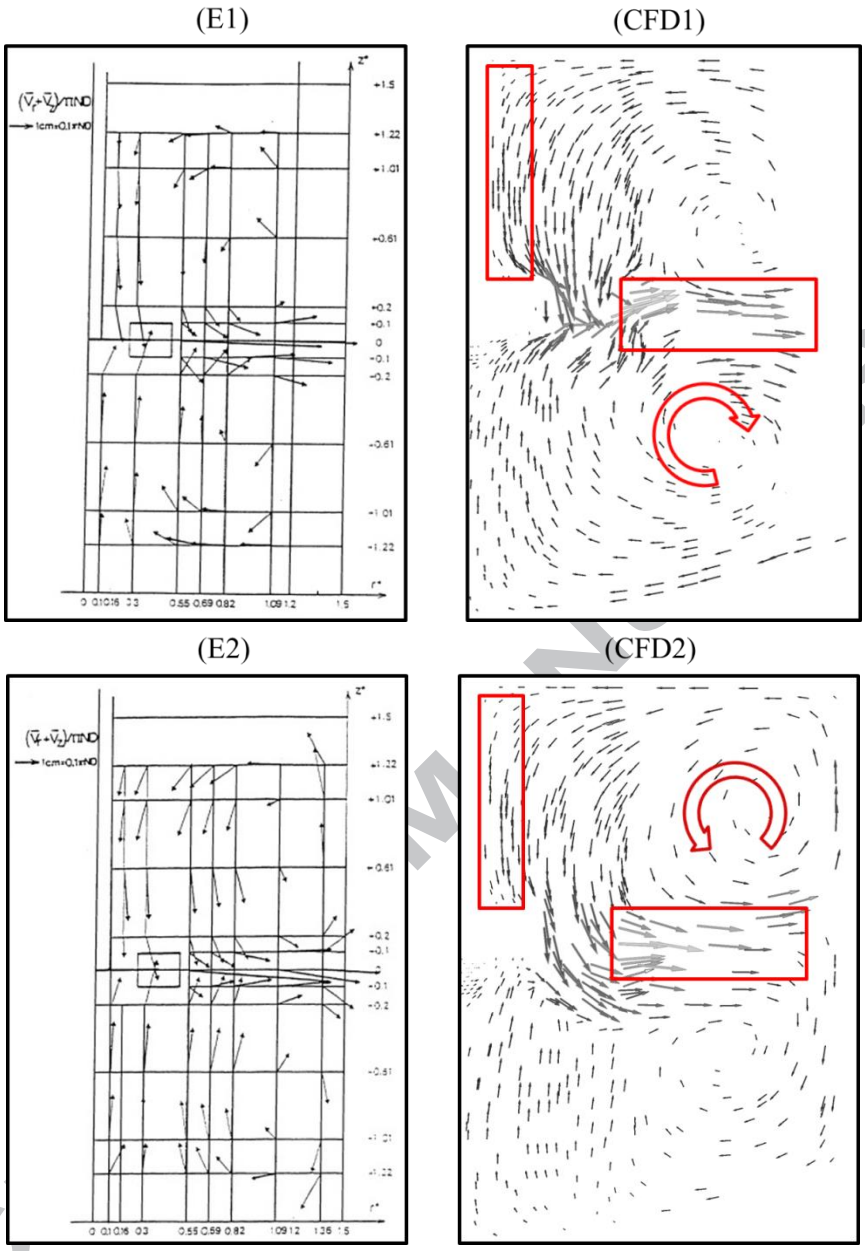

Figure 6. Comparison of experimental results by Costes and Couderc [78] **flow pattern with flow pattern prediction obtained by the CFD model at (E1 and CFD1) vertical plane containing a baffle (θ=0°) and (E2 and CFD2) a vertical plane between baffles (θ=45°)**

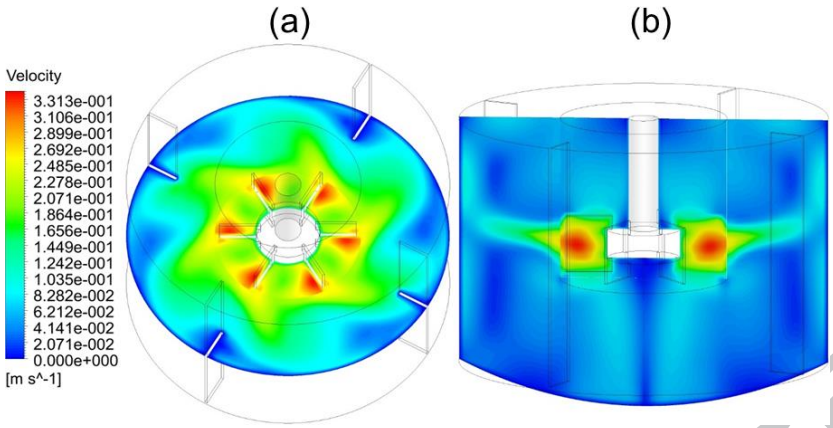

Figure 7. Velocity contours on (a) a horizontal plane at the middle of impeller (b) a vertical symmetry plane

4.3 Crystal Size Distribution (CSD) Variation by Time

CSD was experimentally measured at a number of time intervals: after 3, 10, 20, 30, 40, 50 and 60 min from starting the precipitation (seeding) and the results were compared with the model CSD output in Figure 8.

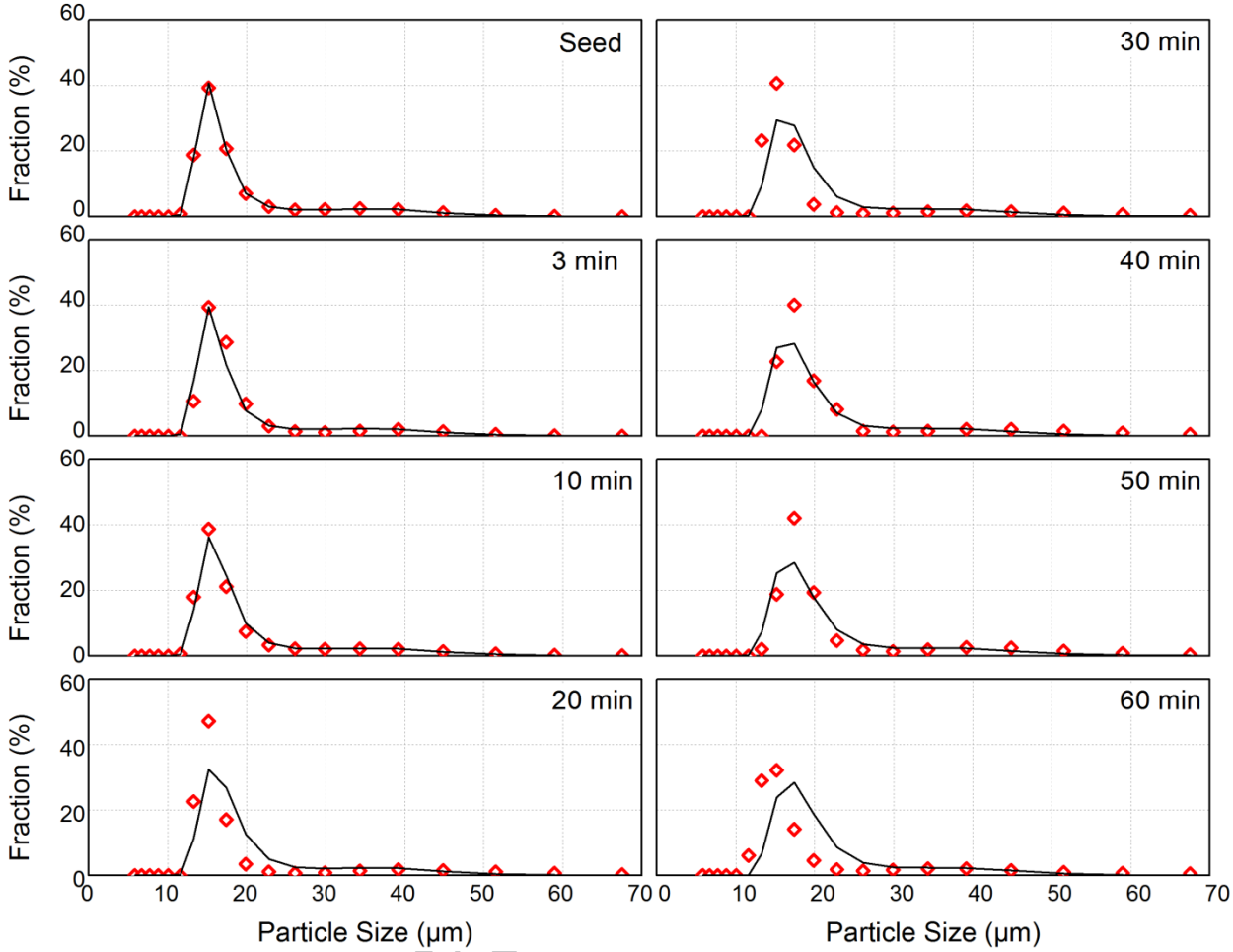

Figure 8. Experimental averaged (◇) and CFD model predicted (——) number fraction based particle size distribution at time = 0 (Seed), 3, 10, 20, 30, 40, 50, and 60 min.

As was demonstrated, the results predicted by the model closely follow the same pattern as the experimental values. In 0 min (Seed) distribution figure, a small discrepancy between model prediction and experimental measurements was observed. This disagreement can be explained as follows: for the initial distribution of particles (or seed size distribution), the software is limited to "volume-based distribution", which was measured by the particle size analyzer. As mentioned earlier, use of the laser scattering particle size analyzer (which initially measures volume-based distribution and then calculates number-based distribution using a

software) may lead to large errors, especially at the lower end of the size range. It is worth pointing out that this numerical error will add on and become part of the errors in the CSD results obtained at later time intervals.

While the magnitudes of the crystal size distribution fractions do not match the experimental results in every case, the shape of the model-predicted distributions is very similar to the experimental results. Also, the position of the peak in each graph—which shows the typical size of crystals at each time interval—is mostly in good agreement with experimental data. The model predicted peak-size percent fraction, which shows the typical size of crystals at each time interval, revealed a deviation from experimental results of 1.42%, 0.05%, 2.43%, 14.6%, 11.2%, 11.7%, 13.6%, and 14.2% at 0, 3, 10, 20, 30, 40, 50, and 60 min, respectively. These deviances could be a combined contribution of: (a) the uncertainties involved in the numerical techniques employed for the coupled CFD-PBM model, and (b) the eccentricities in the experimental results. The present study did not evaluate the individual contributions of the uncertainties from numerical techniques occurring in the CFD and PBM models. Nonetheless, these CSD observations from experimental results and model predictions can be regarded as a positive result given the inherent limitations of the numerical techniques in the models and the uncertainties incurred when sampling reactor crystals. The magnitudes of percent fractions in most of the bins in every time interval are in the reasonable range of experimental error. The percent fractions for other sizes in the distribution, obtained from the model, showed 0 – 20% deviation from experimental results. The mean (μm), standard deviation (μm), and skewness of the model predicted and experimental CSDs after 0, 3, 10, 20, 30, 40, 50 and 60 min are provided in Table S1, showing similar trends. As crystal size increases with experimental time,

the standard deviation and skewness also increases in the experimental condition due to the uncertainties involved in experimental sampling and measurements.

For most cases, the model over-predicts (up to 14%) the size of the crystals in different bins and time intervals, which may be due to the presence of nucleation in the reactor. The nucleation mechanism results in creating finer crystals in comparison with the existing grown crystals. It can be hypothesized here that overlooking nucleation mechanisms and assuming that all the mass transfer resulting from only crystal growth leads to over-prediction of the "*growth/(growth+nucleation)*" ratio in mass transfer; which results in the prediction of larger crystal sizes. The present study did not measure the possible contributions of overlooking of nucleation mechanism and the effect of other uncertainties (i.e. limitations in model numerical calculations and deviations in experimental results) in the observed over-prediction of crystal size by the model.

The experimental data uncertainties (i.e. uncertainties involved in sampling crystals from the reactor) and CSD measurement fluctuations might have become more significant as time passed. This hypothesis, though not validated in this study, is made from the relatively higher degrees of deviations observed in the CSD measurements at times 50 min and 60 min. One possible reason for these variations in experimental data, especially at time 50 min and 60 min could be due to the use of the laser scattering technique to measuring crystal size distribution in the dilute solution. As time passes, and precipitation matures, the solution becomes more cloudless (i.e. more transparent) as compared to initial time solution samples. As a result, the laser scattering particle size analysis technique offers less certainty.

Figure 9 shows the experimental and model predicted average crystal sizes. Since struvite crystals are the product of this process, knowing the average size of the product at different time intervals is an important parameter to control the process and produce products within desirable size range. It can be observed that the averages of the last two experimental measurements (at 50 min and 60 min) were lower than that of the previous observation (at 40 min). This may be due to the fact that there is more chance of breakage of produced crystals during the later stages of the experiment. As the particle size increases, it can break due to collision with baffles, impellers, and each other. So, the average experimental measurements were lower in the last two readings.

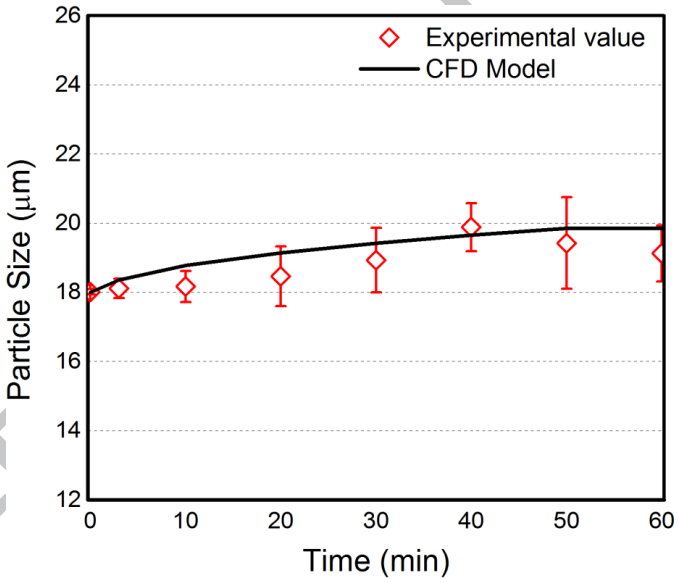

Figure 9. Experimental and CFD predicted particle average size - number fraction weighted

It can be observed that the scatter of the experimental data mostly encompasses the model prediction at different times. Although average crystal size is over-predicted in most cases as

discussed before, it follows the same pattern as real data and the highest error percentage, of about 10%, occurs at time 20 min.

4.4 Supersaturation state Prediction

The results of SI variation over time are compared with the values predicted by CFD model in Figure 10. To find the SI values at every experimental time interval, pH measurement was carried out with extreme care in this study. The total concentration of Mg, N, and P are constant in the reactor. With formation of struvite, elemental concentrations will decline in the liquid phase and increase in the solid phase. Any change in pH will affect the value of SI. Therefore, the value of pH was measured every 5 min from t = 0 (seeding moment) to t = 60 min in all experiments. Then the thermodynamic equilibrium model calculated the SI value from liquid phase elemental concentrations.

The decrease in pH shows that precipitation does occur, since with precipitation, constituent ions will move from liquid phase to solid phase and change the speciation of the solution. Based on equation (1), as struvite precipitates, it releases hydrogen ions in solution, causing a drop in pH. The model predicted pH (via charge balance) and the measured pH values are compared in Figure 10(a) and a maximum deviation of about 0.2 were observed between them. The developed model successfully predicts the SI values with acceptable accuracy. The maximum amount of error was 24%, belonging to the supersaturation index at 60 min.

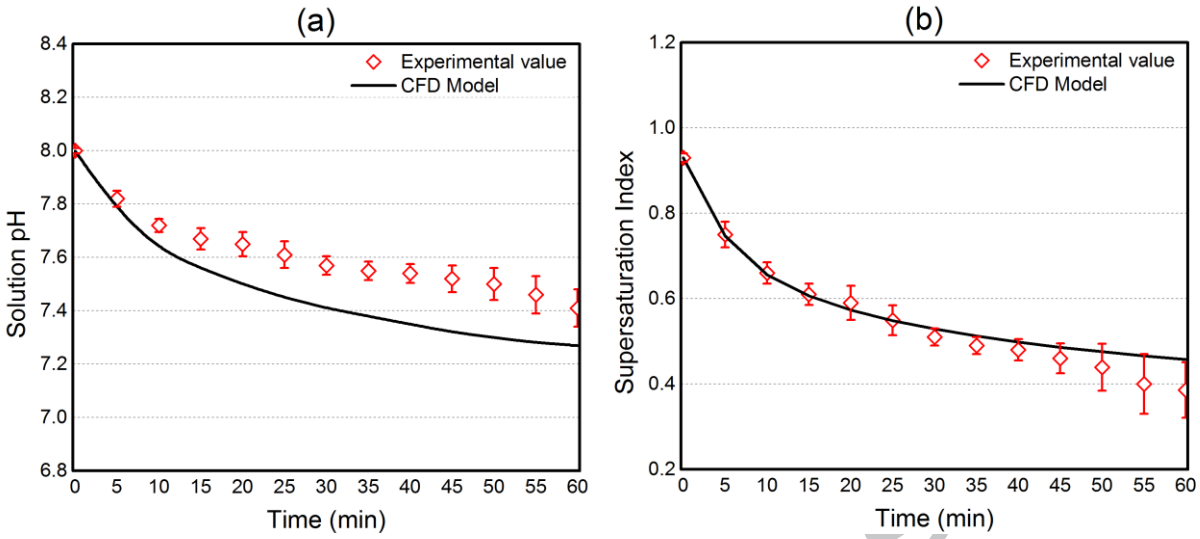

Figure 10. (a) Experimental pH-time variation (b) Experimental and CFD model predicted Supersaturation index-time variation

5. Conclusions

The integrated 3-D CFD-PBM, developed in this study, provides a general approach to obtain CSD of struvite by considering hydrodynamic, thermodynamic, and kinetic aspects of solution chemistry in a batch stirred reactor. Size distribution is essential as it controls a distinct quality of final struvite crystals, which is linked to its commercial application as fertilizer. Hence the development of such general model will enable the design of efficient reactors for the production of specially sized struvite crystals and maximize the economic value of produced fertilizers. The model estimated the time-varying crystal size distribution of particles within an acceptable level of agreement with experimental measurements. Results showed that ignoring nucleation, and considering just the growth phenomena, merged with experimental uncertainties and limitations of the numerical techniques employed for the coupled model, mostly caused over-prediction (up to 14%) of the size of crystals in different time intervals and different size

ranges. As a result, the model though followed the same trend, but over-predicted the average crystal size in the reactor in different time intervals, showing a maximum deviation of 10% at the time of 20 minutes. The general pattern and the position of peaks in CSD curves were found to be in good agreement with the experimental measurements. The model predicted percent fraction for the peak-size, which shows the typical size of crystals at each time interval, revealed a range of 0-14% deviation from experimental observations. Compared to previous attempts, which mostly showed average crystal size, the coupled CFD-PBM model in this study made CSD prediction by considering three different aspects (i.e., hydrodynamic, thermodynamic, and kinetic) of solution chemistry in a stirred reactor. Although not included in this study, it would be interesting to investigate and compare the CSD predictive capabilities of the CFD model against other modeling approaches (e.g., a well-mixed system model). Such a well-mixed system will generalize the hydrodynamic features of the reactor and will reduce computational requirements when compared to CFD models, which was used in the present study. The proximity of model predictions to observed experimental results indicates the suitability of this model in the design of a stirred tank reactor to produce struvite crystals in the desired size range.

Acknowledgements

The authors would like to thank the Natural Science and Engineering Research Council (NSERC) of Canada for providing the financial support required to conduct this study. The authors would also like to acknowledge CalculQuebec and ComputeCanada for providing high-speed computing facility for the present study.

References

[1] UN, Concise Report on the World Population Situation in 2014, United Nations, New York, 2014.

[2] P. Heffer, M. Prud, Fertilizer Outlook 2014-2018, in: 82nd IFA Annual Conference, International Fertilizer Industry Association (IFA), Sydney, Australia, 2014: pp. 1–7.

[3] S. Kataki, H.M. West, M.L. Clarke, D.C. Baruah, Phosphorus recovery as struvite : recent concerns for use of seed , alternative Mg source, nitrogen conservation and fertilizer potential, Resour., Conserv. Recycl. 107 (2016) 142–156.

[4] T. Zhang, L. Ding, H. Ren, Pretreatment of ammonium removal from landfill leachate by chemical precipitation, J. Hazard. Mater. 166 (2009) 911–915. doi:10.1016/j.jhazmat.2008.11.101.

[5] O. Tünay, I. Kabdasli, D. Orhon, S. Kolçak, Ammonia removal by magnesium ammonium phosphate precipitation in industrial wastewaters, Water Sci. Technol. 36 (1997) 225–228. doi:https://doi.org/10.1016/S0273-1223(97)00391-0.

[6] I. Kabdasli, M. Gürel, O. Tünay, Characterization and Treatment of Textile Printing Wastewaters, Environ. Technol. 21 (2000) 1147–1155. doi:10.1080/09593330.2000.9619001.

[7] J.M. Chimenos, A.I. Fernández, G. Villalba, M. Segarra, A. Urruticoechea, B. Artaza, F. Espiell, Removal of ammonium and phosphates from wastewater resulting from the process of cochineal extraction using MgO-containing by-product, Water Res. 37 (2003) 1601–1607. doi:10.1016/S0043-1354(02)00526-2.

[8] M. Türker, I. Çelen, Removal of ammonia as struvite from anaerobic digester effluents and recycling of magnesium and phosphate, Bioresour. Technol. 98 (2007) 1529–1534. doi:10.1016/j.biortech.2006.06.026.

[9] M. Ronteltap, M. Maurer, W. Gujer, Struvite precipitation thermodynamics in source-separated urine, Water Res. 41 (2007) 977–984. doi:10.1016/j.watres.2006.11.046.

[10] R. Yu, J. Geng, H. Ren, Y. Wang, K. Xu, Combination of struvite pyrolysate recycling with mixed-base technology for removing ammonium from fertilizer wastewater, Bioresour. Technol. 124 (2012) 292–298. doi:10.1016/j.biortech.2012.08.015.

[11] N.M. Khai, Chemical Precipitation of Ammonia and Phosphate from Nam Son Landfill Leachate, Hanoi, Iran. J. Energy Environ. 3 (2012) 32–36. doi:10.5829/idosi.ijee.2012.03.05.06.

[12] H. Xu, P. He, W. Gu, G. Wang, L. Shao, Recovery of phosphorus as struvite from sewage sludge ash, J. Environ. Sci. (Beijing, China). 24 (2012) 1533–1538. doi:10.1016/S1001-0742(11)60969-8.

[13] E.L. Foletto, W.R.B. dos Santos, M.A. Mazutti, S.L. Jahn, A. Gündel, Production of struvite from beverage waste as phosphorus source, Mater. Res. (Sao Carlos, Braz.). 16 (2013) 242–245. doi:10.1590/S1516-14392012005000152.

[14] S.G. Barbosa, L. Peixoto, B. Meulman, M.M. Alves, M.A. Pereira, A design of experiments to assess phosphorous removal and crystal properties in struvite precipitation of source separated urine using different Mg sources, Chem. Eng. J. 298 (2016) 146–153. doi:10.1016/j.cej.2016.03.148.

[15] J.A. Wilsenach, C.A.H. Schuurbiers, M.C.M. van Loosdrecht, Phosphate and potassium recovery from source separated urine through struvite precipitation, Water Res. 41 (2007) 458–466. doi:10.1016/j.watres.2006.10.014.

[16] Q. Zhao, T. Zhang, C. Frear, K. Bowers, J. Harrison, S. Chen, Phosphorous recovery technology in conjunction with dairy anaerobic digestion., CSANR Research Report 2010-001, 2010. http://csanr.wsu.edu/publications/researchreports/cffreport.html.

[17] M.S. Rahaman, D.S. Mavinic, A. Meikleham, N. Ellis, Modeling phosphorus removal and recovery from anaerobic digester supernatant through struvite crystallization in a fluidized bed reactor, Water Res. 51 (2014) 1–10. doi:10.1016/j.watres.2013.11.048.

[18] A. Guadie, S. Xia, W. Jiang, L. Zhou, Z. Zhang, S.W. Hermanowicz, X. Xu, S. Shen, Enhanced struvite recovery from wastewater using a novel cone-inserted fluidized bed reactor, J. Environ. Sci. (Beijing, China). 26 (2014) 765–774. doi:10.1016/S1001-0742(13)60469-6.

[19] C.C. Su, R.R.M. Abarca, M.D.G. de Luna, M.C. Lu, Phosphate recovery from fluidized-bed wastewater by struvite crystallization technology, J. Taiwan Inst. Chem. Eng. 45 (2014) 2395–2402. doi:10.1016/j.jtice.2014.04.002.

[20] M.I. Ali, P.A. Schneider, An approach of estimating struvite growth kinetic incorporating thermodynamic and solution chemistry, kinetic and process description, Chem. Eng. Sci. 63 (2008) 3514–3525. doi:10.1016/j.ces.2008.04.023.

[21] L. Pastor, D. Mangin, R. Barat, A. Seco, A pilot-scale study of struvite precipitation in a stirred tank reactor: Conditions influencing the process, Bioresour. Technol. 99 (2008)

6285–6291. doi:10.1016/j.biortech.2007.12.003.

[22] M. Hanhoun, L. Montastruc, C. Azzaro-Pantel, B. Biscans, M. Frèche, L. Pibouleau, Simultaneous determination of nucleation and crystal growth kinetics of struvite using a thermodynamic modeling approach, Chem. Eng. J. 215–216 (2013) 903–912. doi:10.1016/j.cej.2012.10.038.

[23] Z. Wang, Z. Mao, C. Yang, X. Shen, Computational Fluid Dynamics Approach to the Effect of Mixing and Draft Tube on the Precipitation of Barium Sulfate in a Continuous Stirred Tank1, Chin. J. Chem. Eng. 14 (2006) 713–722. doi:http://dx.doi.org/10.1016/S1004-9541(07)60001-9.

[24] D. Logashenko, T. Fischer, S. Motz, E.D. Gilles, G. Wittum, Simulation of crystal growth and attrition in a stirred tank, Comput. Visualization Sci. 9 (2006) 175–183. doi:10.1007/s00791-006-0031-z.

[25] Z. Sha, P. Oinas, M. Louhi-Kultanen, G. Yang, S. Palosaari, Application of CFD simulation to suspension crystallization—factors affecting size-dependent classification, Powder Technol. 121 (2001) 20–25. doi:10.1016/S0032-5910(01)00369-2.

[26] Z. Zhu, H. Wei, Flow field of stirred tank used in the crystallization process of ammonium sulphate, ScienceAsia. 34 (2008) 97–101. doi:10.2306/scienceasia1513-1874.2008.34.097.

[27] W. Wantha, A.E. Flood, Numerical simulation and analysis of flow in a DTB crystallizer, Chem. Eng. Commun. 195 (2008) 1345–1370. doi:10.1080/00986440801963527.

[28] R. Plewik, P. Synowiec, J. Wojcik, A. Kus, Suspension flow in crystallizers with and

without hydraulic classification, Chem. Eng. Res. Des. 88 (2010) 1194–1199. https://www.cheric.org/research/tech/periodicals/view.php?seq=852693.

[29] M.S. Rahaman, D.S. Mavinic, Recovering nutrients from wastewater treatment plants through struvite crystallization: CFD modelling of the hydrodynamics of UBC MAP fluidized-bed crystallizer, Water Sci. Technol. 59 (2009) 1887–1892. doi:10.2166/wst.2009.214.

[30] M. Al-Rashed, J. Wójcik, R. Plewik, P. Synowiec, A. Kuś, Multiphase CFD modeling: Fluid dynamics aspects in scale-up of a fluidized-bed crystallizer, Chem. Eng. Process. 63 (2013) 7–15. doi:10.1016/j.cep.2012.11.001.

[31] C. V. Rane, A.A. Ganguli, E. Kalekudithi, R.N. Patil, J.B. Joshi, D. Ramkrishna, CFD simulation and comparison of industrial crystallizers, Can. J. Chem. Eng. 92 (2014) 2138–2156. doi:10.1002/cjce.22078.

[32] Z. Jaworski, A.W. Nienow, CFD modelling of continuous precipitation of barium sulphate in a stirred tank, Chem. Eng. J. 91 (2003) 167–174. doi:10.1016/S1385-8947(02)00150-X.

[33] M.S. Rahaman, M.R. Choudhury, A.S. Ramamurthy, D.S. Mavinic, N. Ellis, F. Taghipour, CFD modeling of liquid-solid fluidized beds of polydisperse struvite crystals, Int. J. Multiphase Flow. 99 (2018) 48–61. doi:10.1016/j.ijmultiphaseflow.2017.09.011.

[34] K.N. Ohlinger, T.M. Young, E.D. Schroeder, Predicting struvite formation in digestion, Water Res. 32 (1998) 3607–3614. doi:10.1016/S0043-1354(98)00123-7.

[35] I. Çelen, J.R. Buchanan, R.T. Burns, R. Bruce Robinson, D. Raj Raman, Using a chemical equilibrium model to predict amendments required to precipitate phosphorus as struvite in

liquid swine manure, Water Res. 41 (2007) 1689–1696. doi:10.1016/j.watres.2007.01.018.

[36] M.S. Rahaman, D.S. Mavinic, N. Ellis, Phosphorus recovery from anaerobic digester supernatant by struvite crystallization: Model-based evaluation of a fluidized bed reactor, Water Sci. Technol. 58 (2008) 1321–1327. doi:10.2166/wst.2008.721.

[37] M. Hanhoun, L. Montastruc, C. Azzaro-Pantel, B. Biscans, M. Frèche, L. Pibouleau, Temperature impact assessment on struvite solubility product: A thermodynamic modeling approach, Chem. Eng. J. 167 (2011) 50–58. doi:10.1016/j.cej.2010.12.001.

[38] N.J. Barnes, A.R. Bowers, A probabilistic approach to modeling struvite precipitation with uncertain equilibrium parameters, Chem. Eng. Sci. 161 (2017) 178–186. doi:10.1016/j.ces.2016.12.026.

[39] N.C. Bouropoulos, P.G. Koutsoukos, Spontaneous precipitation of struvite from aqueous solutions, J. Cryst. Growth. 213 (2000) 381–388. doi:10.1016/S0022-0248(00)00351-1.

[40] N.O. Nelson, R.L. Mikkelsen, D.L. Hesterberg, Struvite precipitation in anaerobic swine lagoon liquid: Effect of pH and Mg:P ratio and determination of rate constant, Bioresour. Technol. 89 (2003) 229–236. doi:10.1016/S0960-8524(03)00076-2.

[41] M. Quintana, E. Sánchez, M.F. Colmenarejo, J. Barrera, G. García, R. Borja, Kinetics of phosphorus removal and struvite formation by the utilization of by-product of magnesium oxide production, Chem. Eng. J. 111 (2005) 45–52. doi:10.1016/j.cej.2005.05.005.

[42] K.S. Le Corre, E. Valsami-Jones, P. Hobbs, S.A. Parsons, Kinetics of struvite precipitation: Effect of the magnesium dose on induction times and precipitation rates, Environ. Technol. 28 (2007) 1317–1324. doi:10.1080/09593332808618891.

[43] M. Quintana, M.F. Colmenarejo, J. Barrera, E. Sánchez, G. García, L. Travieso, R. Borja, Removal of phosphorus through struvite precipitation using a by-product of magnesium oxide production (BMP): Effect of the mode of BMP preparation, Chem. Eng. J. 136 (2008) 204–209. doi:10.1016/j.cej.2007.04.002.

[44] M.S. Rahaman, N. Ellis, D.S. Mavinic, Effects of various process parameters on struvite precipitation kinetics and subsequent determination of rate constants, Water Sci. Technol. 57 (2008) 647–654. doi:10.2166/wst.2008.022.

[45] E. Ariyanto, T.K. Sen, H.M. Ang, The influence of various physico-chemical process parameters on kinetics and growth mechanism of struvite crystallisation, Adv. Powder Technol. 25 (2014) 682–694. doi:10.1016/j.apt.2013.10.014.

[46] A. Capdevielle, E. Sýkorová, F. Béline, M.L. Daumer, Kinetics of struvite precipitation in synthetic biologically treated swine wastewaters, Environ. Technol. 35 (2014) 1250–1262. doi:10.1080/09593330.2013.865790.

[47] N.-M. Chong, Q.-M. Thai, Optimization and kinetics of nutrient removal from wastewater by chemical precipitation of struvite, Desalin. Water Treat. 54 (2015) 3422–3431. doi:10.1080/19443994.2014.908416.

[48] M.I.H. Bhuiyan, D.S. Mavinic, R.D. Beckie, Nucleation and growth kinetics of struvite in a fluidized bed reactor, J. Cryst. Growth. 310 (2008) 1187–1194. doi:10.1016/j.jcrysgro.2007.12.054.

[49] M.. Harrison, M.R. Johns, E.T. White, C.M. Mehta, Growth Rate Kinetics for Struvite Crystallisation, Chemical Engineering Transactions. 25 (2011) 309–314.

doi:10.3303/CET1125052.

[50] A. Triger, J.S. Pic, C. Cabassud, Determination of struvite crystallization mechanisms in urine using turbidity measurement, Water Res. 46 (2012) 6084–6094. doi:10.1016/j.watres.2012.08.030.

[51] C.M. Mehta, D.J. Batstone, Nucleation and growth kinetics of struvite crystallization, Water Res. 47 (2013) 2890–2900. doi:10.1016/j.watres.2013.03.007.

[52] S.C. Galbraith, P.A. Schneider, A.E. Flood, Model-driven experimental evaluation of struvite nucleation, growth and aggregation kinetics, Water Res. 56 (2014) 122–132. doi:10.1016/j.watres.2014.03.002.

[53] D. Crutchik, J.M. Garrido, Kinetics of the reversible reaction of struvite crystallisation, Chemosphere. 154 (2016) 567–572. doi:10.1016/j.chemosphere.2016.03.134.

[54] S. Qamar, Modeling and Simulation of Population Balances for Particulate Processes, Faculty of Mathematics, Otto-von-Guericke University Magdeburg, 2008.

[55] S. Qamar, G. Warnecke, M.P. Elsner, A. Seidel-Morgenstern, A Laplace transformation based technique for reconstructing crystal size distributions regarding size independent growth, Chemical Engineering Science. 63 (2008) 2233–2240. doi:10.1016/j.ces.2008.01.025.

[56] S.C. Galbraith, P.A. Schneider, Modelling and simulation of inorganic precipitation with nucleation, crystal growth and aggregation: A new approach to an old method, Chem. Eng. J. 240 (2014) 124–132. doi:10.1016/j.cej.2013.11.070.

[57] C.W. Childs, C.W. Childs, A Potentiometric Study of Equilibria in Aqueous Divalent

Metal Orthophosphate Solutions, Inorganic Chemistry. 9 (1970) 2465–2469. doi:10.1021/ic50093a017.

[58] M.M. François, J.G.H. Morel, Principles and Application of Aquatic Chemistry, 1993.

[59] A.W. Taylor, A.W. Frazier, E.L. Gurney, Solubility products of magnesium ammonium and magnesium potassium phosphates, Trans. Faraday Soc. 59 (1963) 1580–1584. doi:10.1039/tf9635901580.

[60] A.E. Martell, R.M. Smith, Critical Stability Constants, Plenum Press, New York, London, 1974.

[61] V.L. Snoeyink, D. Jenkins, Water Chemistry, Wiley, USA, 1980.

[62] J.W. Mullin, Crystallization, 3rd ed., Butterworth-Heinemann, 1993.

[63] M.S. Rahaman, Phosphorus Recovery from Wastewater through Struvite Crystallization in a Fluidized Bed Reactor: Kinetics, Hydrodynamics and Performance, The University of British Columbia, 2009.

[64] K.N. Ohlinger, T.M. Young, E.D. Schroeder, Kinetics Effects on Preferential Struvite Accumulation in Wastewater, J. Environ. Eng. 125 (1999) 730–737.

[65] M.I. Ali, P.A. Schneider, A fed-batch design approach of struvite system in controlled supersaturation, Chem. Eng. Sci. 61 (2006) 3951–3961. doi:10.1016/j.ces.2006.01.028.

[66] A.G. Jones, Crystallization Process Systems, 1st ed., Butterworth-Heinemann, Boston, 2002.

[67] C. V. Rane, E. Kalekudithi, J.B. Joshi, D. Ramkrishna, Effect of Impeller Design and

Power Consumption on Crystal Size Distribution, AIChE J. 60 (2014) 3596–3613. doi:10.1002/aic.14541.

[68] J.B. Joshi, V. V. Ranade, Computational fluid dynamics for designing process equipment: Expectations, current status, and path forward, Ind. Eng. Chem. Res. 42 (2003) 1115–1128. doi:10.1021/ie0206608.

[69] D. Ramkrishna, Population balances, 1st ed., Academic Press, 2000. doi:10.1016/B978-012576970-9/50000-X.

[70] M.J. Hounslow, R.L. Ryall, V.R. Marshall, A discretized population balance for nucleation, growth, and aggregation, AIChE J. 34 (1988) 1821–1832. doi:10.1002/aic.690341108.

[71] J.D. Lister, D.J. Smit, M.J. Hounslow, Adjustable discretized population balance for growth and aggregation, AIChE J. 41 (1995) 591–603. doi:10.1002/aic.690410317.

[72] S. Srisanga, A.E. Flood, S.C. Galbraith, S. Rugmai, S. Soontaranon, J. Ulrich, Crystal growth rate dispersion versus size-dependent crystal growth: Appropriate modeling for crystallization processes, Crystal Growth and Design. 15 (2015) 2330–2336. doi:10.1021/acs.cgd.5b00126.

[73] A. Brucato, M. Ciofalo, F. Grisafi, G. Micale, Numerical prediction of flow fields in baffled stirred vessels: A comparison of alternative modelling approaches, Chem. Eng. Sci. 53 (1998) 3653–3684. doi:10.1016/S0009-2509(98)00149-3.

[74] C. Bartels, M. Breuer, K. Wechsler, F. Durst, Computational fluid dynamics applications on parallel-vector computers: Computations of stirred vessel flows, Comput. Fluids. 31

(2002) 69–97. doi:10.1016/S0045-7930(01)00016-0.

[75] D.A. Deglon, C.J. Meyer, CFD modelling of stirred tanks: Numerical considerations, Miner. Eng. 19 (2006) 1059–1068. doi:10.1016/j.mineng.2006.04.001.

[76] J.H. Rushton, E.W. Costich, H.J. Everett, Power characteristics of mixing impellers -Part II, Chem. Eng. Prog. 46 (1950) 467–476.

[77] J.M. Zalc, M.M. Alvarez, F.J. Muzzio, B.E. Arik, Extensive validation of computed laminar flow in a stirred tank with three Rushton turbines, AIChE J. 47 (2001) 2144–2154. doi:10.1002/aic.690471003.

[78] J. Costes, J.P. Couderc, Study by laser Doppler anemometry of the turbulent flow induced by a Rushton turbine in a stirred tank: Influence of the size of the units—I. Mean flow and turbulence, Chem. Eng. Sci. 43 (1988) 2751–2764. doi:https://doi.org/10.1016/0009-2509(88)80018-6.

[79] D. Wadnerkar, M.O. Tade, V.K. Pareek, R.P. Utikar, CFD simulation of solid–liquid stirred tanks for low to dense solid loading systems, Particuology. 29 (2016) 16–33. doi:10.1016/j.partic.2016.01.012.

3-D CFD-PBM coupled modeling and experimental investigation of struvite precipitation in a batch stirred reactor

Seyyed Ebrahim Mousavi, Mahbuboor Rahman Choudhury, Md. Saifur Rahaman*

Department of Building, Civil, and Environmental Engineering, Concordia University, 1455 de Maisonneuve Blvd, West, Montreal, Quebec, Canada H3G 1M8

*Corresponding Author: Email: saifur.rahaman@concordia.ca; Tel.: +1-514-848-2424, Ext. 5058.

Highlights

- A 3D CFD-PBM model developed to predict struvite formation in batch stirred reactor
- Includes hydrodynamic, thermodynamic, kinetic variables of struvite precipitation
- Crystal size distribution obtained from model matches experimental results
- Model will aid efficient reactor design for production of desired struvite crystals